



## RESEARCH LETTER

10.1002/2016GL071349

## Key Points:

- Upper ocean submesoscale (here 10–100 km) turbulence and inertia-gravity waves undergo strong seasonal cycles that are out of phase
- Submesoscale turbulence dominates the horizontal velocity and sea surface height variability in late winter/early spring
- Submesoscale inertia-gravity waves dominate the horizontal velocity and sea surface height variability in late summer/early fall

## Supporting Information:

- Supporting Information S1

## Correspondence to:

C. B. Rocha,  
crocha@ucsd.edu

## Citation:

Rocha, C. B., S. T. Gille, T. K. Chereskin, and D. Menemenlis (2016), Seasonality of submesoscale dynamics in the Kuroshio Extension, *Geophys. Res. Lett.*, 43, 11,304–11,311, doi:10.1002/2016GL071349.

Received 16 JUL 2016

Accepted 19 OCT 2016

Accepted article online 25 OCT 2016

Published online 8 NOV 2016

## Seasonality of submesoscale dynamics in the Kuroshio Extension

Cesar B. Rocha<sup>1</sup>, Sarah T. Gille<sup>1</sup>, Teresa K. Chereskin<sup>1</sup>, and Dimitris Menemenlis<sup>2</sup>

<sup>1</sup>Scripps Institution of Oceanography, University of California San Diego, La Jolla, California, USA, <sup>2</sup>Earth Sciences Division, Jet Propulsion Laboratory, California Institute of Technology, Pasadena, California, USA

**Abstract** Recent studies show that the vigorous seasonal cycle of the mixed layer modulates upper ocean submesoscale turbulence. Here we provide model-based evidence that the seasonally changing upper ocean stratification in the Kuroshio Extension also modulates submesoscale (here 10–100 km) inertia-gravity waves. Summertime restratification weakens submesoscale turbulence but enhances inertia-gravity waves near the surface. Thus, submesoscale turbulence and inertia-gravity waves undergo vigorous out-of-phase seasonal cycles. These results imply a strong seasonal modulation of the accuracy of geostrophic velocity diagnosed from submesoscale sea surface height delivered by the Surface Water and Ocean Topography satellite mission.

## 1. Introduction

Recent interest in upper ocean dynamics has focused on the strong seasonal cycle of shallow baroclinic instabilities and their role in submesoscale (roughly 1–100 km) turbulence and mesoscale (roughly 100–300 km) modulation [Sasaki *et al.*, 2014; Qiu *et al.*, 2014; Brannigan *et al.*, 2015; Callies *et al.*, 2015; Thompson *et al.*, 2016; Buckingham *et al.*, 2016]. Contemporary studies have also shown that inertia-gravity waves (IGWs) contribute significantly to the near-surface variability at submesoscales [Richman *et al.*, 2012; Bühler *et al.*, 2014; Rocha *et al.*, 2016], but their seasonality has not been investigated.

The partition between geostrophic and ageostrophic flows across the submesoscales and their seasonality have immediate applications for the planning of the Surface Water and Ocean Topography (SWOT) satellite mission. SWOT will deliver sea surface height (SSH) with about 15 km resolution, thereby providing the first global SSH measurements at submesoscales [Fu and Ubelmann, 2014]. Thus, the projection of energetic submesoscale ageostrophic flows, such as inertia-gravity waves (IGWs), onto SSH represents a challenge and an opportunity for the SWOT community. The challenge is how to diagnose submesoscale surface velocity from SSH. The opportunity is stimulation of research on interactions between geostrophic and ageostrophic flows and their projection onto SSH.

Using the output of two comprehensive global numerical simulations, here we show that IGWs undergo a strong near-surface seasonal cycle in the Kuroshio Extension region. Interestingly, the seasonal cycle of IGWs is out of phase with the seasonal cycle of submesoscale turbulence. Consistent with previous studies, submesoscale turbulence is strongest in winter [Sasaki *et al.*, 2014; Qiu *et al.*, 2014]. IGWs with horizontal scales between 10 and 100 km (hereafter submesoscale IGWs), however, peak in late summer/early fall, when the upper ocean is strongly stratified. Thus, there exists a strong seasonal modulation of upper ocean submesoscale dynamics: submesoscale turbulence dominates the upper ocean dynamics in late winter/early fall, whereas submesoscale IGWs prevail in late summer/early fall.

## 2. The LLC Numerical Simulations

We use results of two latitude-longitude polar cap (LLC) comprehensive numerical simulations. The outputs analyzed here, LLC2160 (nominal resolution  $1/24^\circ \approx 4.7$  km; effective resolution  $\approx 20$  km) and LLC4320 (nominal resolution  $1/48^\circ \approx 2.3$  km; effective resolution  $\approx 8$  km), are forward solutions of the Massachusetts Institute of Technology general circulation model (MITgcm) [Marshall *et al.*, 1997] on a LLC grid [Forget *et al.*, 2015] with 90 vertical levels. The coarser-resolution LLC simulation was spun up from an Estimating the Circulation and Climate of the Ocean, Phase II (ECCO2) [Menemenlis *et al.*, 2008] adjoint-method state estimate, constrained to millions of observations from 2009 to 2011.

The LLC2160 output spans 2 years from March 2011 to April 2013; the LLC4320 was spun up from the LLC2160 simulation, spanning 1 year from September 2011 to October 2012. Both LLC2160 and LLC4320 simulations were forced by tides hourly and by 6-hourly surface atmospheric fields. The LLC4320 simulation is an extension of the 3 month long output used by *Rocha et al.* [2016]—for details, see supporting information.

Tidal forcing by the 16 most significant components represents a key feature of the LLC2160 and LLC4320 simulations. Barotropic tides flowing over topography convert significant tidal energy into the internal wave field. Those internal waves project onto mesoscales to submesoscales [e.g., *Rocha et al.*, 2016]. Hence, tidal forcing fundamentally distinguishes our analysis from other modeling studies of seasonality [*Sasaki et al.*, 2014; *Qiu et al.*, 2014].

To study seasonal variations in the upper ocean dynamics, we focus on the northwest Pacific, in the vicinity of the Kuroshio Extension, where previous studies have shown strong mesoscale and submesoscale seasonality [*Sasaki et al.*, 2014; *Qiu et al.*, 2014]. We analyze a subdomain of the LLC4320 and LLC2160 simulations of about 2000 km<sup>2</sup> spanning 155–175°E; 25–40°N (Figure 1a). The stratification in this mesoscale-rich subtropical region undergoes a vigorous seasonal cycle: wintertime-enhanced small-scale turbulence destratifies the upper ocean, yielding mixed layers deeper than 200 m to the north (Figure 1b). Summertime restratification yields mixed layers shallower than 40 m (Figure 1c).

Fundamentally, the upper ocean density structure is well captured by both LLC simulations: a comparison with Argo climatology (updated from *Roemmich and Gilson* [2009]) shows that both simulations skillfully represent the Kuroshio Extension stratification and its seasonal variability (supporting information). Moreover, model smoothed fields have eddy kinetic energy (EKE) levels (0.041 m<sup>2</sup> s<sup>-2</sup>) similar to Jason II across-track geostrophic EKE (0.036 m<sup>2</sup> s<sup>-2</sup>) and gridded geostrophic EKE (0.032 m<sup>2</sup> s<sup>-2</sup>).

### 3. Bulk Statistics of the Surface Lateral Velocity Gradient Tensor

To study the seasonality in the surface velocity, we calculate the lateral velocity gradient tensor

$$\begin{bmatrix} u_x & u_y \\ v_x & v_y \end{bmatrix} \quad (1)$$

using a centered second-order finite difference scheme—we obtain qualitatively similar results using spectral differentiation of velocity fields periodized with reflections; statistics of fields obtained via spectral differentiation are 10–15% larger. We then diagnose the vertical vorticity

$$\zeta \equiv v_x - u_y, \quad (2)$$

lateral rate of strain

$$\alpha \equiv \left[ (u_x - v_y)^2 + (u_y + v_x)^2 \right]^{1/2}, \quad (3)$$

and horizontal divergence

$$\delta \equiv u_x + v_y. \quad (4)$$

Because vortices, fronts, and IGWs are ubiquitous at submesoscales, second-order statistics of vorticity, strain, and divergence highlight these fine lateral scales [e.g., *Shcherbina et al.*, 2013].

The model solutions depict seasonality in vorticity (Figures 1d and 1e): large values of fine-grained vertical vorticity are observed in early spring with maximum values as large as  $4f$ , where  $f$  is the local planetary vorticity, and root-mean-square (RMS) of about  $0.4f$ . In early fall, the situation is the opposite: the vertical vorticity is relatively coarse grained; its local maximum and RMS are both smaller than  $0.5f$ . Indeed, the vorticity and rate of strain are strongest in wintertime (Figure 2): in both simulations, the RMS vorticity and strain rate are about twice as large in late winter/early spring than in late summer/early fall. Because the wintertime vorticity and strain rate are dominated by the smallest scales in the flow (the KE spectrum is shallower than a  $-3$  power law in winter), increasing the resolution from  $1/24^\circ$  to  $1/48^\circ$  increases the wintertime RMS vorticity and strain by about 40%.

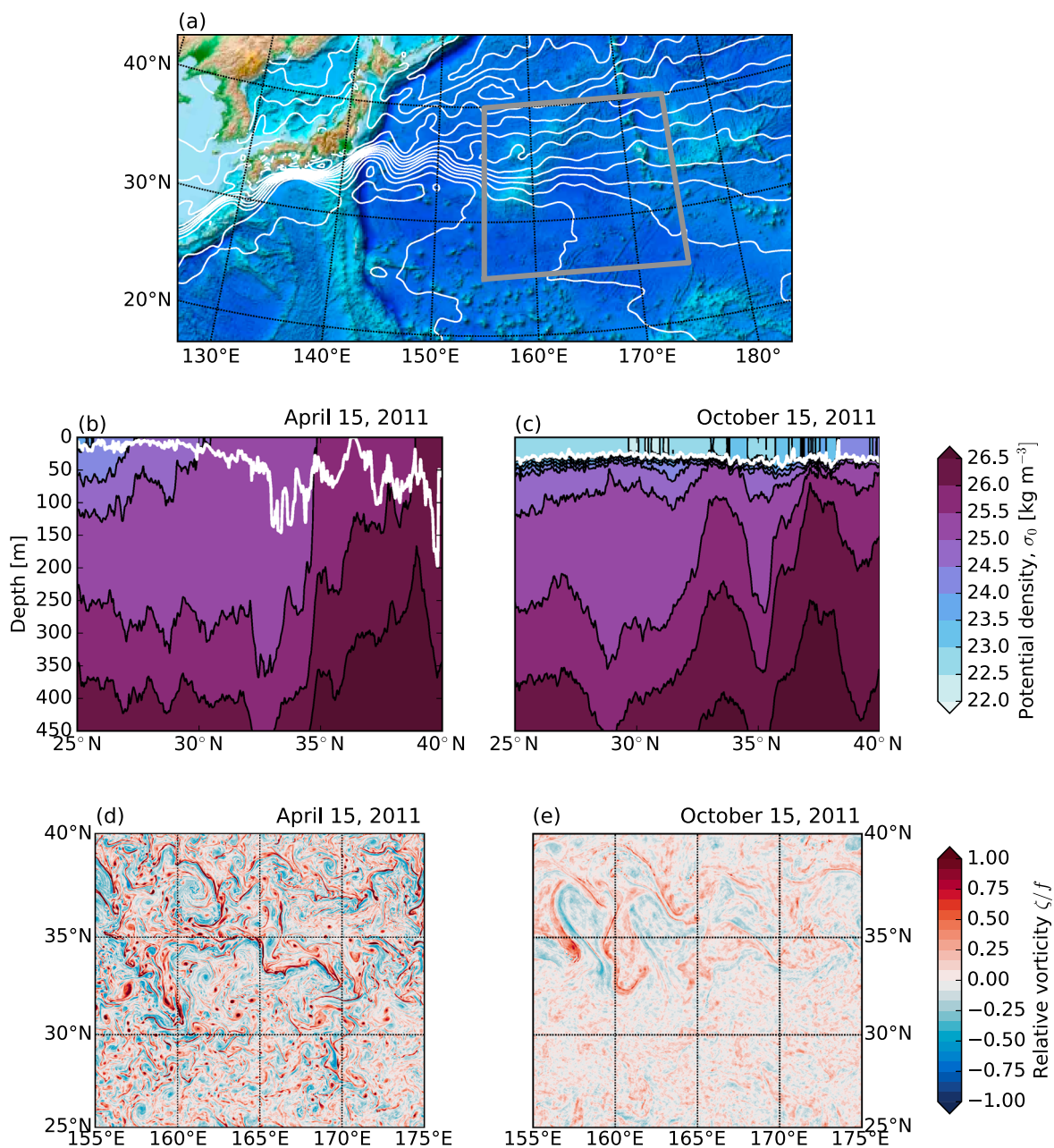


**Figure 1.** (a) The study region with the subregion where the LLC outputs are analyzed. Colors represent the topography and white lines are contours of absolute dynamic topography every 0.1 m from AVISO. LLC 4320 (1/48°) snapshots of transects of (b, c) potential density at 165°E and (d, e) surface vorticity. In Figures 1b and 1c the white line represents the mixed layer depth. The snapshots were taken at 12:00 UTC.

Subinertial flows account for the bulk of vertical vorticity and strain rate ( $T_{32.5} = 2\pi/f_{32.5} \approx 22.3$  h, where  $f_{32.5}$  is the inertial frequency at the midlatitude 32.5°N): daily averaging the velocity fields suppresses superinertial motions and reduces the RMS vorticity by 40% and the RMS strain by 10%; the seasonal cycle remains strong (see dashed lines in Figures 2a and 2b). Indeed, submesoscale flows account for most of this seasonal cycle: smoothing the velocity fields with a Hanning filter with cutoff scale of 100 km dramatically reduces the RMS vorticity and strain rate. The reduction in variance is about 80% in winter, yielding RMS vorticity and strain rate roughly consistent with the diagnostics from AVISO-gridded geostrophic velocities (compare red lines to black lines in Figures 2a and 2b). The picture that emerges is consistent with recent studies: shallow baroclinic instabilities energize the submesoscales in winter, drawing from the available potential energy stored in large lateral buoyancy gradients in deep mixed layers [Sasaki et al., 2014; Callies et al., 2015, 2016].

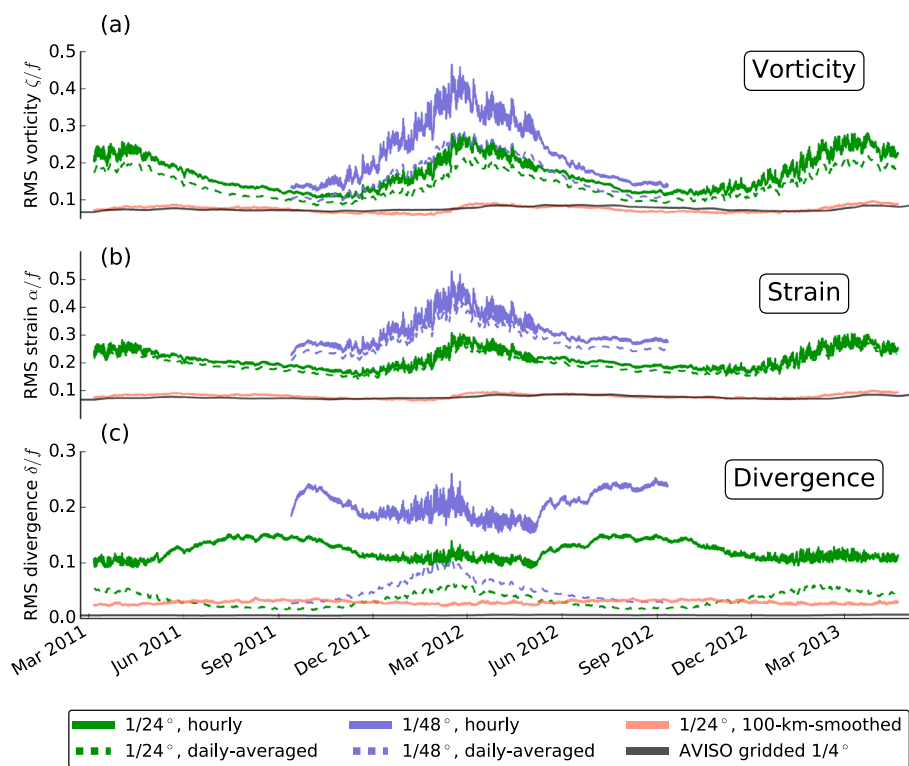


**Figure 2.** Time series of the root-mean-square (RMS) of surface (a) vorticity, (b) rate of strain, and (c) horizontal divergence in the LLC outputs and gridded AVISO data. The convergence of meridians account for the small RMS divergence in AVISO line in Figure 2c.

The seasonal cycle of the horizontal divergence, however, showcases the complexity of the upper ocean annual variability. If submesoscale turbulence dominated the near-surface variability all year, then the seasonal cycle of horizontal divergence, vertical vorticity, and lateral strain rate would be in phase [e.g., Sasaki *et al.*, 2014]. While there is a clear wintertime peak in divergence of daily averaged velocity (see dashed lines in Figure 2c; RMS divergence  $\sim 0.1f$  in the  $1/48^\circ$  simulation), the hourly fields show a stronger enhancement of lateral divergence in late summer/early fall (RMS divergence  $\sim 0.22f$  in the  $1/48^\circ$  simulation). Because the  $1/48^\circ$  simulation better resolves smaller-scale submesoscale flows, a secondary RMS divergence peak in winter is nearly as strong as in summer. Submesoscale fronts and eddies evolve relatively fast, and there is no clear temporal and spatial scale separation between those motions and IGWs [McWilliams, 2016]: daily averaging the velocity fields efficiently suppresses the summertime horizontally divergent flows and also reduces the wintertime lateral divergence by about 50%. Figure 2c also shows that most of the lateral divergence is associated with submesoscale flows: smoothing the velocity fields with a 100 km cutoff suppresses more than 80% of the RMS divergence.

#### 4. Joint Probability Density Functions

The results of Figures 2a–2c show that submesoscale surface variability stems from different dynamics in summer than in winter. To characterize these differences, we calculate joint probability distributions (joint PDF) of vorticity-strain and vorticity-Laplacian of sea surface height (Figure 3).

The April vorticity-strain joint PDF has a shape characteristic of submesoscale turbulence (Figures 3a and 3b). The alignment of vorticity and strain  $\alpha \sim \pm\zeta$  with strong positive skewness are fingerprints of submesoscale fronts [Shcherbina *et al.*, 2013; McWilliams, 2016]. The shape of the vorticity-strain joint PDF is similar for hourly and daily averaged fields, although the vorticity skewness reduces from 1.4 to 1.13 from hourly to daily averaged. The April results indicate that wintertime submesoscale surface velocity is strongly dominated by submesoscale turbulence. The daily averaged fields are largely in geostrophic balance, but the hourly velocity and sea surface height fields have an important ageostrophic component as depicted by the joint PDF of vorticity-Laplacian of SSH winter (Figure 3e).

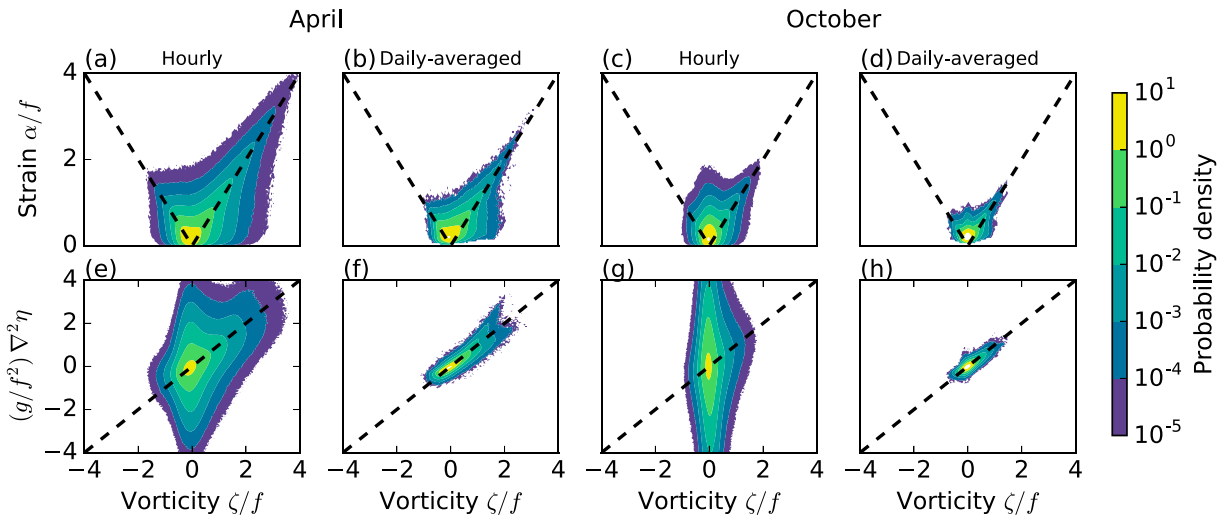


**Figure 3.** Seasonal variation of joint probability distributions of surface lateral velocity gradient tensor: (a–d) vorticity versus strain rate, and (e–h) vorticity versus Laplacian of sea surface height in April (Figures 3a, 3b, 3e, and 3f) and October (Figures 3c, 3d, 3g, and 3h). Dashed lines in Figures 3a–3d represent one-dimensional shear flow  $\alpha = \pm\zeta$ , characteristic of fronts. Dashed lines in Figures 3e–3h represent geostrophic flow  $\zeta = \frac{g}{f^2} \nabla^2 \eta$ .

The October vorticity-strain joint PDF shows much weaker skewness (the vorticity skewness is 0.68 and 0.67 for hourly and daily averaged velocities). The shape of the vorticity-strain joint PDF appears to be a combination of two half ellipses centered about  $\zeta = 0$ , one with a 45° slope (characteristic of submesoscale fronts that persist in summer) and one with a very steep slope. That the submesoscale dynamics in October are mainly ageostrophic is clearly depicted in the shape of the joint PDF of vorticity-Laplacian of sea surface height for hourly fields (Figure 3g), which is an ellipse aligned in the vertical axis. Daily averaging the model suppresses the ageostrophic, superinertial flows, and therefore, the daily averaged flow is essentially geostrophic as depicted by the 45°-tilted ellipse in the vorticity-Laplacian of sea surface height joint PDF (Figure 3h).

Time series of PDFs of vorticity and divergence (supporting information) show a strong oscillation between these two regimes. In late winter/early spring the vorticity is strongly positively skewed, whereas the divergence is moderately negatively skewed (convergence/downwelling) as predicted by frontogenesis [e.g., McWilliams, 2016]. In late summer/early fall, the divergence is stronger, but PDFs are much less skewed, consistent with a superposition of random linear IGWs [e.g., Garrett and Munk, 1972].

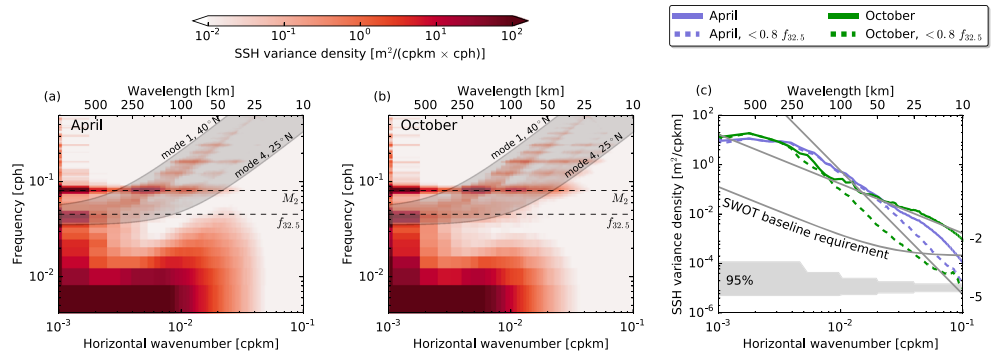


**Figure 4.** LLC4320 wave number-frequency spectrum of SSH variance in (a) April and (b) October. (c) Wave number spectrum of SSH variance—the integral of Figures 4a and 4b over frequency. In Figures 4a and 4b, the light gray shaded region depicts the dispersion relations for inertia-gravity waves from mode 1 through mode 4 across the latitudinal domain; horizontal dashed lines represent the semidiurnal lunar tidal frequency ( $M_2$ ) and the inertial frequency at midlatitude ( $f_{32.5}$ ). For reference, the gray line shows the baseline requirement as specified by the SWOT science team [Rodríguez, 2014].

**Table 1.** The Square Root of the Mean-Square SSH at Submesoscales (10–100 km) Estimated From the Wave Number-Frequency Spectrum of SSH Variance in Figure 4<sup>a</sup>

	April	October
Subinertial ( $< 0.8f$ )	5.2 cm	2.0 cm
Superinertial ( $> 1.2f$ )	2.9 cm	4.9 cm
Near- $f$ ( $0.8–1.2f$ )	0.3 cm	0.4 cm
Near- $M_2$ ( $0.8–1.2M_2$ )	1.5 cm	3.1 cm

<sup>a</sup>The SWOT baseline requirement at 15 km is approximately  $\sqrt{2}$  cm.

## 5. Wave Number-Frequency Spectrum

To confirm that submesoscale IGWs account for most of the superinertial SSH variance and surface KE, we calculate the wave number-frequency spectrum of SSH variance. Focusing on the high-frequency content, we compute the wave number-frequency spectrum every 10 days and average the results to obtain a spectral estimate. Before calculating the discrete Fourier transform, we remove linear trends and multiply the data by a three-dimensional Hanning window. We azimuthally average the spectrum in wave number.

Mesoscale flows and the lunar semidiurnal tide contain most of the SSH variance (Figures 4a and 4b). But there is a significant SSH variance at submesoscales, both subinertial and superinertial. Subinertial SSH variance at submesoscales is larger in April, whereas superinertial SSH variance at submesoscales is larger in October. At scales smaller than 100 km (submesoscales), the SSH variance is 66% larger in October than in April. IGWs, particularly modes 2 through 4, account for most of the SSH variance increase in summer—higher vertical modes are more sensitive to changes in near-surface stratification (supporting information). In October, superinertial IGWs account for a SSH standard deviation of about 4.9 cm, comparable to the April subinertial SSH standard deviation of  $\sim 5.2$  cm (Table 1). Similarly, the submesoscale superinertial surface KE is 63% larger in October than in April (supporting information).

Figure 4c shows the integral over frequency of wave number-frequency spectra in Figures 4a and 4b. Both in April and October, the SSH wave number spectrum approximately follows a  $-2$  power law at submesoscales (solid lines in Figure 4c)—there is a small difference between the spectra owing to the phase cancellation between the seasonal cycle of submesoscale turbulence and IGWs. The subinertial flow has a steeper submesoscale SSH variance wave number spectrum (dashed lines in Figure 4c). The difference between the SSH variance wave number spectrum for all frequencies and subinertial frequencies is dramatic in October when superinertial flows account for about 80% of the SSH variance and KE at submesoscales—we obtain similar results by computing SSH variance and KE wave number spectra directly from hourly and daily averaged SSH velocity fields.

## 6. Discussion and Conclusion

Our work adds to recent model [e.g., *Sasaki et al.*, 2014] and observational [e.g., *Callies et al.*, 2015; *Buckingham et al.*, 2016] evidence of vigorous seasonality in submesoscale turbulence. In particular—in global simulations with embedded tides—near-surface submesoscale IGWs undergo a strong seasonal cycle that is out of phase with the seasonal cycle of submesoscale turbulence. IGW energy and SSH variance are significantly spread across the submesoscales, likely through mesoscale advection and refraction, and dispersion [e.g., *Ponte and Klein*, 2015; *Alford et al.*, 2016, and references therein] and parametric subharmonic instability (PSI) [e.g., *MacKinnon and Winters*, 2005], though the LLC simulations are unlikely to fully resolve PSI. In the LLC simulations, superinertial IGWs account for most of the surface submesoscale KE and SSH variance; near-inertial IGWs project onto larger scales, possibly because submesoscale NIWs quickly propagate into the interior and weakly project onto SSH.

*D'Asaro* [1978] showed that the velocity of linear internal waves in the mixed layer strongly depends on the density jump at the mixed layer base, with largest velocities when the jump is strongest. In summer, the shallow mixed layer overlays a strong seasonal pycnocline, and thus the internal waves projection onto the mixed layer may be stronger according to *D'Asaro's* [1978] arguments. An alternative explanation is that

the shape of the baroclinic modes changes seasonally (see World Ocean Atlas 2013, *Levitus et al.* [2013], and modal shapes in the supporting information).

Internal tide energy flux does not show a seasonal modulation [e.g., *Alford*, 2003]; hence, one expects a strong seasonality in the near-surface expression of internal tides and higher-frequency IGWs if the near-surface stratification varies strongly. The intermittent windy near-inertial wave (NIW) generation peaks in early winter, but NIW energy has a similar energy level in October and April [*Alford et al.*, 2016]. Furthermore, in our simulations the higher-frequency inertia-gravity waves account for most of the seasonality in superinertial surface KE and SSH (Figures 4a and 4b).

The seasonally varying mixed layer depth challenges observation and simulation of flows at mixed layer deformation radius length scale in observational programs and models with fixed resolution [*Buckingham et al.*, 2016]. But the mixed layer available potential energy is lowest in summer owing to shallow mixed layer depths and weak lateral buoyancy gradients [*Callies et al.*, 2015]. Moreover, in baroclinic turbulence, the deformation radius has only a secondary, catalytic role—most of the baroclinic conversion occurs at larger scales [*Larichev and Held*, 1995; *Callies et al.*, 2016]. Thus, the model failure to resolve the summertime mixed layer deformation radius is unlikely to account for the vigorous seasonality in submesoscale turbulence.

In the context of SWOT, these results imply that if one is interested only in the geostrophic flow, so that surface velocity can be diagnosed from SSH, then the signal-to-noise ratio will have a strong seasonality owing to the presence of IGWs (the coherent fraction of internal tides may be removed efficiently). An important caveat is that the Kuroshio Extension may be typical of a mesoscale-rich subtropical regions, but it is unlikely to be representative of other regions such as low-eddy kinetic energy eastern boundary currents. We plan to report on the geographic variability of submesoscale seasonality in a future study.

#### Acknowledgments

William R. Young and three reviewers provided helpful and stimulating comments. Greg Wagner suggested that the near-surface shape of the baroclinic modes changes seasonally. We thank the MITgcm community and our colleagues at the NASA Advanced Supercomputing (NAS) Division for their awesome support. This research was funded by NSF (OCE1357047) and NASA (NNX13AE44G, NNX13AE85G, NNX16AH67G, and NNX16AO5OH). The LLC output can be obtained from the ECCO project ([http://ecco2.org/llc\\_hires](http://ecco2.org/llc_hires)). The altimeter products were produced by Ssalto/Duacs and distributed by AVISO, with support from CNES (<http://www.aviso.altimetry.fr/duacs/>). Codes and output files are available online at the project repository (<https://github.com/crocha700/UpperOceanSeasonality>).

#### References

- Alford, M. H. (2003), Redistribution of energy available for ocean mixing by long-range propagation of internal wave, *Nature*, *423*(6936), 159–162.
- Alford, M. H., J. A. MacKinnon, H. L. Simmons, and J. D. Nash (2016), Near-inertial internal gravity waves in the ocean, *Annu. Rev. Mar. Sci.*, *8*, 95–123.
- Brannigan, L., D. P. Marshall, A. Naveira-Garabato, and A. G. Nurser (2015), The seasonal cycle of submesoscale flows, *Ocean Modell.*, *92*, 69–84.
- Buckingham, C. E., A. C. Naveira Garabato, A. F. Thompson, L. Brannigan, A. Lazar, D. P. Marshall, A. George Nurser, G. Damerell, K. J. Heywood, and S. E. Belcher (2016), Seasonality of submesoscale flows in the ocean surface boundary layer, *Geophys. Res. Lett.*, *43*, 2118–2126, doi:10.1002/2016GL068009.
- Bühler, O., J. Callies, and R. Ferrari (2014), Wave–vortex decomposition of one-dimensional ship-track data, *J. Fluid Mech.*, *756*, 1007–1026.
- Callies, J., R. Ferrari, J. M. Klymak, and J. Gula (2015), Seasonality in submesoscale turbulence, *Nat. Commun.*, *6*, 6862.
- Callies, J., G. Flierl, R. Ferrari, and B. Fox-Kemper (2016), The role of mixed-layer instabilities in submesoscale turbulence, *J. Fluid Mech.*, *788*, 5–41.
- D'Asaro, E. A. (1978), Mixed layer velocities induced by internal wave, *J. Geophys. Res.*, *83*(C5), 2437–2438.
- Forget, G., J.-M. Campin, P. Heimbach, C. Hill, R. Ponte, and C. Wunsch (2015), ECCO version 4: An integrated framework for non-linear inverse modeling and global ocean state estimation, *Geosci. Model Dev.*, *8*, 3071–3104.
- Fu, L.-L., and C. Ubelmann (2014), On the transition from profile altimeter to swath altimeter for observing global ocean surface topography, *J. Atmos. Oceanic Technol.*, *31*(2), 560–568.
- Garrett, C., and W. Munk (1972), Space-time scales of internal waves, *Geophys. Astrophys. Fluid Dyn.*, *3*(1), 225–264.
- Larichev, V. D., and I. M. Held (1995), Eddy amplitudes and fluxes in a homogeneous model of fully developed baroclinic instability, *J. Phys. Oceanogr.*, *25*(10), 2285–2297.
- Levitus, S., et al. (2013), The world ocean database, *Data Sci. J.*, *12*, WDS229–WDS234.
- MacKinnon, J., and K. Winters (2005), Subtropical catastrophe: Significant loss of low-mode tidal energy at 28.9°, *Geophys. Res. Lett.*, *32*, L15605, doi:10.1029/2005GL023376.
- Marshall, J., C. Hill, L. Perelman, and A. Adcroft (1997), Hydrostatic, quasi-hydrostatic, and nonhydrostatic ocean modeling, *J. Geophys. Res.*, *102*(C3), 5733–5752.
- McWilliams, J. C. (2016), Submesoscale currents in the ocean, *Philos. Trans. R. Soc. London, Ser. A*, *472*, doi:10.1098/rspa.2016.0117.
- Menemenlis, D., J.-M. Campin, P. Heimbach, C. Hill, T. Lee, A. Nguyen, M. Schodlok, and H. Zhang (2008), ECCO2: High resolution global ocean and sea ice data synthesis, *Mercator Ocean Q. Newsl.*, *31*, 13–21.
- Ponte, A. L., and P. Klein (2015), Incoherent signature of internal tides on sea level in idealized numerical simulations, *Geophys. Res. Lett.*, *42*, 1520–1526, doi:10.1002/2014GL062583.
- Qiu, B., S. Chen, P. Klein, H. Sasaki, and Y. Sasai (2014), Seasonal mesoscale and submesoscale eddy variability along the North Pacific Subtropical Countercurrent, *J. Phys. Oceanogr.*, *44*(12), 3079–3098.
- Richman, J. G., B. K. Arbic, J. F. Shriver, E. J. Metzger, and A. J. Wallcraft (2012), Inferring dynamics from the wavenumber spectra of an eddying global ocean model with embedded tides, *J. Geophys. Res.*, *117*, C12012, doi:10.1029/2012JC008364.
- Rocha, C. B., T. K. Chereskin, S. T. Gille, and D. Menemenlis (2016), Mesoscale to submesoscale wavenumber spectra in Drake Passage, *J. Phys. Oceanogr.*, *46*, 601–620.
- Rodriguez, E. (2014), *Surface Water and Ocean Topography Mission (SWOT): Science Requirements Document*, SWOT NASA/JPL Project, Pasadena, Calif. [Available at [https://swot.jpl.nasa.gov/files/swot/SRD\\_021215.pdf](https://swot.jpl.nasa.gov/files/swot/SRD_021215.pdf)].
- Roemmich, D., and J. Gilson (2009), The 2004–2008 mean and annual cycle of temperature, salinity, and steric height in the global ocean from the Argo Program, *Prog. Oceanogr.*, *82*(2), 81–100.

- Sasaki, H., P. Klein, B. Qiu, and Y. Sasai (2014), Impact of oceanic-scale interactions on the seasonal modulation of ocean dynamics by the atmosphere, *Nat. Commun.*, *5*, 5636.
- Shcherbina, A. Y., E. A. D'Asaro, C. M. Lee, J. M. Klymak, M. J. Molemaker, and J. C. McWilliams (2013), Statistics of vertical vorticity, divergence, and strain in a developed submesoscale turbulence field, *Geophys. Res. Lett.*, *40*, 4706–4711, doi:10.1002/grl.50919.
- Thompson, A. F., A. Lazar, C. Buckingham, A. C. Naveira Garabato, G. M. Damerell, and K. J. Heywood (2016), Open-ocean submesoscale motions: A full seasonal cycle of mixed layer instabilities from gliders, *J. Phys. Oceanogr.*, *46*(4), 1285–1307.